Wang, H., Sun, Y., Lühr, H. (2024): Interplanetary Magnetic Field By Effects on the Strength and Latitude of Field-Aligned Currents in Different Magnetic Local Time Sectors. - Journal of Geophysical Research: Space Physics, 129, 2, e2023JA032188.

https://doi.org/10.1029/2023JA032188

JGR Space Physics

RESEARCH ARTICLE
10.1029/2023JA032188

Interplanetary Magnetic Field B_y Effects on the Strength and Latitude of Field-Aligned Currents in Different Magnetic Local Time Sectors

Hui Wang[1], Yu Sun[1], and Hermann Lühr[2]

[1]Department of Space Physics, School of Electronic Information, Wuhan University, Wuhan, China, [2]German Research Centre for Geosciences, GFZ, Potsdam, Germany

Key Points:

- At dusk and 09–14 MLT with eastward polar electrojet, the northern (southern) FACs are stronger when IMF $B_y < 0$ ($B_y > 0$)
- At dawn, 21–02 MLT, and 09–14 MLT with westward polar electrojet, the northern (southern) FACs are stronger when IMF $B_y > 0$ ($B_y < 0$)
- Northern (southern) FACs with eastward electrojet are located at higher latitude for IMF $B_y > 0$ ($B_y < 0$), while FACs with westward electrojet show reverse variation

Supporting Information:

Supporting Information may be found in the online version of this article.

Correspondence to:

H. Wang,
h.wang@whu.edu.cn

Citation:

Wang, H., Sun, Y., & Lühr, H. (2024). Interplanetary magnetic field B_y effects on the strength and latitude of field-aligned currents in different magnetic local time sectors. *Journal of Geophysical Research: Space Physics*, *129*, e2023JA032188. https://doi.org/10.1029/2023JA032188

Received 16 OCT 2023
Accepted 30 JAN 2024

Abstract In this work, IMF B_y effects on field-aligned currents (FACs) are examined in different local time sectors, seasons, and hemispheres. At dusk and 09–14 MLT, when the eastward polar electrojet (PEJ) prevails, the northern FACp (poleward side FACs) are stronger when IMF $B_y < 0$ than when IMF $B_y > 0$. Conversely, at dawn, 21–02 MLT, and 09–14 MLT with westward PEJ, the northern FACp are stronger with IMF $B_y > 0$ compared to IMF $B_y < 0$. The southern FACp shows a reversed relationship with IMF B_y direction. The dependence of FACe (equatorward side FACs) on IMF B_y is weaker, except for the midday FACe, which shows opposite variations with respect to IMF B_y when compared to FACp. Stronger IMF B_y effect is observed in local summer in most of local times. The northern FACs are located at higher latitude for IMF $B_y > 0$ than for IMF $B_y < 0$ in local times with eastward PEJ, while the opposite trend is observed in other local times and in the Southern Hemisphere. The hemispheric difference in the peak latitude of FACs demonstrates an inverse relationship with its intensity, with stronger FACs located at lower latitudes. Overall, the local time and hemispheric differences in FACs strength and latitude are discussed in the context of interhemispheric field-aligned currents linked to IMF B_y.

1. Introduction

Field-aligned currents (FACs) play an important role in the magnetosphere-ionosphere coupling system. They remain a hot topic in space weather since satellite observations confirmed their existences (e.g., Friis-Christensen & Wilhjelm, 1975; Iijima & Potemra, 1976; Vennerstrøm et al., 2002, 2005; Wang & Lühr, 2023; Wang et al., 2005, 2014). Region 1 (R1) FACs flows into the ionosphere on the dawn side and out of the ionosphere on the dusk side. Region 2 (R2) FACs are located on the equatorward side of R1 FACs and show reversed flow direction. R1 FACs originate from the magnetopause and magnetotail lobe region, while R2 FACs originate from the ring current in the inner magnetosphere (e.g., Sato & Iijima, 1979). When the interplanetary magnetic field (IMF) is directed northward, one pair of FACs emerge in the polar cap, termed as NBZ FACs, which show opposite polarity to that of R1 FACs. NBZ FACs is related to the nightside lobe reconnection (e.g., Vennerstrøm et al., 2002; Wang et al., 2008). When IMF $B_y > 0$ (oriented duskward), two distinct patches of FACs appear in the cusp region, recognized as DPY (Dayside Polar cap Y) FACs (Clauer & Friis-Christensen, 1988). The poleward part of DPY FACs (termed as midday R0 FACs) flows out of the ionosphere in the Northern Hemisphere (NH), while the equatorward part of DPY FACs (termed as midday R1 FACs) shows opposite flow direction. The situation gets reversed when IMF $B_y < 0$ (oriented dawnward). The dependence of DPY FACs on IMF B_y sign is reverse in the Southern Hemisphere (SH) (Erlandson et al., 1988; Iijima & Potemra, 1982).

The FACs intensity is effectively controlled by the solar wind merging electric field, E_m, which characterizes the combined influence of IMF B_y and B_z magnitudes, and is symmetrical with respect to the polarity of the IMF B_y component (e.g., Cheng et al., 2018; Huang et al., 2017; Kervalishvili and Lühr, 2014; Wang et al., 2005). However, the hemispheric differences in the auroral intensities and electromagnetic energy input have been revealed to depend on the orientation of IMF B_y and solar illumination (e.g., Hu et al., 2014; Liou & Mitchell, 2020; Liu et al., 2020; Østgaard et al., 2011; Pakhotin et al., 2021). In a comprehensive analysis conducted by Hu et al. (2014) using long-term and multi-spectral auroral observations in the Arctic and Antarctica, it was revealed that when IMF B_y was positive (negative), the auroral intensities at 557.7 and 630.0 nm emissions in the SH (NH) were more intense in the afternoon compared to negative (positive) IMF B_y conditions. Additionally, Holappa et al. (2020) observed a higher electron precipitation flux at dawn and midnight for IMF $B_y > 0$ in the NH winter, compared to that for IMF $B_y < 0$; the reversed IMF B_y effect was observed during the

SH winter. Furthermore, Holappa et al. (2021) reported that the IMF B_y effect on upward FACs and auroral electrojets was more pronounced in the dawn sector and negligible at dusk, with noon and nighttime not covered in their work. It is generally agreed that upward FACs are linked to electron precipitation (e.g., Knight, 1973; Korth et al., 2014), and a positive correlation exists between upward/downward FACs and particle precipitation (e.g., Robinson et al., 2020; Wang & Zou, 2022). Thus, it is expected that FACs show hemispheric and local time differences in the dependence on the polarity of IMF B_y, although this has so far not been verified by satellite in situ observations.

Recent studies have reported a seasonal dependence of the IMF B_y effect on aurora activity. For instance, Reistad et al. (2020) determined that for a constant level of solar wind input, the polar cap expanded and the magnetic activity intensified when IMF B_y and dipole tilt angle (DPT) had opposite signs, that is, for IMF $B_y > 0$ and a negative DPT (NH winter) or IMF $B_y < 0$ and a positive DPT (NH summer). This suggests that the IMF B_y effect at high latitudes remains equally strong in both the summer and winter hemispheres, because the IMF B_y component modulates the dayside reconnection rate and the global energy input into the magnetosphere, as indicated by Reistad et al. (2021). Consequently, the ionospheric current system might be stronger for IMF $B_y > 0$ during the December solstice (DeceS) and for IMF $B_y < 0$ during the June solstice (JuneS) in both the summer and winter hemispheres, responding to increased global magnetospheric convection. In contrast to this perspective, an IMF B_y effect on the auroral westward electrojet, represented by the auroral AL index, was reported to be most prominent during NH winter (Friis-Christensen et al., 2017; Holappa et al., 2021; Holappa & Mursula, 2018; Laundal et al., 2018; Smith et al., 2017). Workayehu et al. (2021) determined that the most pronounced IMF B_y effect on hemispheric integrated ionospheric currents occurred during the local winter seasons. In NH winter, the total integrated curl-, divergence-free currents and FACs in the auroral region were approximately 20%–35% larger for IMF $B_y > 0$ compared to that for IMF $B_y < 0$. The IMF B_y effect on SH currents had reversed signs but remained more substantial in local winter. It is worth noting that in the study of Workayehu et al. (2021), integrated FACs were calculated without differentiation between upward and downward FACs. In the current research, we will investigate the behavior of FACs on the poleward and equatorward sides in response to IMF B_y sign.

This study is the first to conduct a detailed investigation of the influence of the IMF B_y component on peak FACs strength and latitude in different local time sectors, seasons, and hemispheres, using observations of the Swarm satellites. The data and methodology used in this study are described in Section 2. The statistical analysis of the observations is presented in Sections 3 and 4. A discussion and summary in the context of previous publications are presented in Sections 5 and 6.

2. Data and Processing Method

The three Swarm satellites were launched into a near-polar orbit with an inclination of 87.5° on 22 November 2013. The final orbit constellation was achieved on 17 April 2014. Swarm A and C maintained a longitudinal separation of 1.4° at approximately 450 km, while Swarm B circled at about 530 km. Swarm A and C covered all the local time sectors in about 133 days. Swarm satellites were equipped with both scalar and vector magnetometers, enabling measurements of magnetic field with high accuracy.

FACs are determined from the vector magnetic field data of Swarm A and C by employing Ampere's integral law: $j_{\parallel} = \frac{1}{\mu_0 A \sin(i)} \oint \mathrm{B dl}$. The integral is conducted along a closed path encompassing the measurement quad, which includes the connecting lines between the orbit segments of Swarm A and C (see Figure 6.2 of Lühr et al., 2020). To determine the disturbance magnetic field B in the horizontal plane, the CHAOS-6 model is employed to subtract the background magnetic field. Here, dl represents a line element along the integration path, A signifies the area of a closed quad formed by four observation points, I denotes the magnetic field inclination angle, and μ_0 corresponds to the vacuum permeability. In order to eliminate small-scale FAC structures of less than 150 km, we apply a low-pass filter with a cutoff period of 20 s to the magnetic field data (please refer to Lühr et al. (2020) and Ritter et al. (2013) for more information). In the following text positive FACs refer to currents flowing out of the ionosphere, and negative FACs refers to currents flowing into the ionosphere. FACs with absolute values less than 50 $\mu A/m^2$ are considered for outlier rejection.

The scalar magnetic field data of Swarm A were used to deduce ionospheric polar electrojets (PEJs). The line current method for estimation of PEJ was initially proposed by Olsen (1996). This method has been subsequently

applied to CHAMP data (Ritter et al., 2013) and Swarm data by Aakjær et al. (2016). The CHAMP PEJ was verified through comparisons with ground-based observations (Ritter et al., 2004). The PEJ is approximated by a collection of infinite line currents situated in the E layer of ionosphere, spaced at 1° interval. The observed total field residuals are inverted to derive the strength of each line current, by leveraging a least square fitting approach. In this work positive PEJ denotes eastward currents, and negative PEJ denotes westward current. The absolute values of the peaks are required to be within 0.03 A/m and 3 A/m for preventing false detections. The Apex latitudes were used for FACs that mapped the observation point along magnetic field lines down to the E region and quasi-dipole (QD) latitudes for PEJ (e.g., Emmert et al., 2010; Richmond, 1995). This approach allows for a direct comparison of FACs and PEJ at the same magnetic coordinates within the E region.

Six years' worth of Swarm-A PEJ and dual-spacecraft Swarm A-C FACs, spanning from 17 April 2014 to 16 April 2020 are used in the present work. Beyond this timeframe, the reliability of high-latitude dual-spacecraft FAC estimates diminishe due to the changing constellation during the Counter-Rotating Orbits phase. For each satellite's passage from 50° MLat to the pole, eastward PEJ peaks at 15–20 MLT, and westward PEJ peaks at 21–02 MLT and 03–08 MLT are documented. Statistically, around noon, the averaged eastward PEJ occur for IMF $B_y > 0$, whereas the averaged westward PEJ for IMF $B_y < 0$. This is consistent with the characteristics of DPY currents (e.g., Friis-Christensen et al., 1985; Huang et al., 2017). Thus, both eastward and westward PEJ peaks are selected separately at 09–14 MLT, contingent upon the direction of duskward or dawnward IMF B_y. In this study, the merging electric field E_m (after Newell et al., 2007), IMF B_y and B_z are all calculated as an average within 10 and 20 min before detecting the peak of PEJ, allowing for the propagation of IMF effect from the bow shock to the ionosphere (e.g., Huang et al., 2017). Figure S1 in Supporting Information S1 file shows one example of PEJ as observed when Swarm traversed the duskside aurora region around 14 UT on 16 July 2014. The top panel shows the temporal variation of IMF B_y from 13 UT to 14.3 UT, while the bottom panel shows PEJ as a function of MLat. The black dashed line indicates the UT corresponding to the peak eastward PEJ. The blue double dashed lines indicate the time interval utilized for averaging IMF B_y, which is 10–20 min before the peak PEJ detection.

This article is a follow-on work of our previous research (Wang & Lühr, 2023, 2024), wherein we employed a consistent 6-hr MLT interval. The motivation for using such a broad MLT bin width is to ensure sufficient statistics in all MLT bins. It is worth noting that Holappa et al. (2020) analyzed the electron flux data in three different MLT bins, each spanning 8 hr: 20–04 MLT (night), 04–12 MLT (dawn), and 12–20 MLT (dusk) in order to study potential MLT dependence of electron flux on IMF B_y effect. Additionally, Holappa and Buzulukova (2022) studied the IMF B_y effect on the energetic proton flux specifically in the dusk sector, focusing on the 12 to 24 MLT interval. In this work, the MLT of peak PEJ is used to define the events, following previous works (e.g., Wang & Lühr, 2023, 2024).

The event numbers of auroral crossings are shown in Figure 1, categorized by hemisphere, season, and local time bin. We define two seasons as: June solstice (spanning 66 days before and after July 1), and December solstice (covering 66 days before and after January 1). Overall, the situation is more favorable in the Northern Hemisphere with typically more than 840 events per bin. In the Southern hemisphere significant parts of the high magnetic latitudes are not well sampled, due to the large offset of the magnetic pole. The distance between the geographic and magnetic poles is more than double as large in the Southern as in the Northern Hemisphere. This affects, in particular, the noontime sector where part of the FACs are located in the polar cap. Nevertheless, across each MLT bin, the number of events generally surpasses 200, ensuring the reliability of the statistical study. At 09–14 MLT, while the eastward (westward) PEJ predominantly exists for IMF $B_y > 0$ (IMF $B_y < 0$) in the NH, it is noteworthy that there exist hundreds of cases where eastward PEJ occur for IMF $B_y < 0$, and vice versa in the SH. Thus, in the present work, the dependence of the noontime eastward (westward) PEJ on the polarity of IMF B_y are compared in a manner consistent with other local time sectors.

3. Average Current Density Profiles

Through the application of a superposed location analysis, PEJ and FACs data are sorted into 2° ΔMLat bins. The key latitude, ΔMLat = 0°, is determined by the peak PEJ. Averages over all current density profiles of PEJ and FACs, centered at the key latitude, are calculated. These averages are generated separately for four MLT sectors and for two Lloyd seasons: June solstice, and December solstice. This meticulous methodology allows us to effectively elucidate the latitude variations within auroral current systems associated with aurora activity.

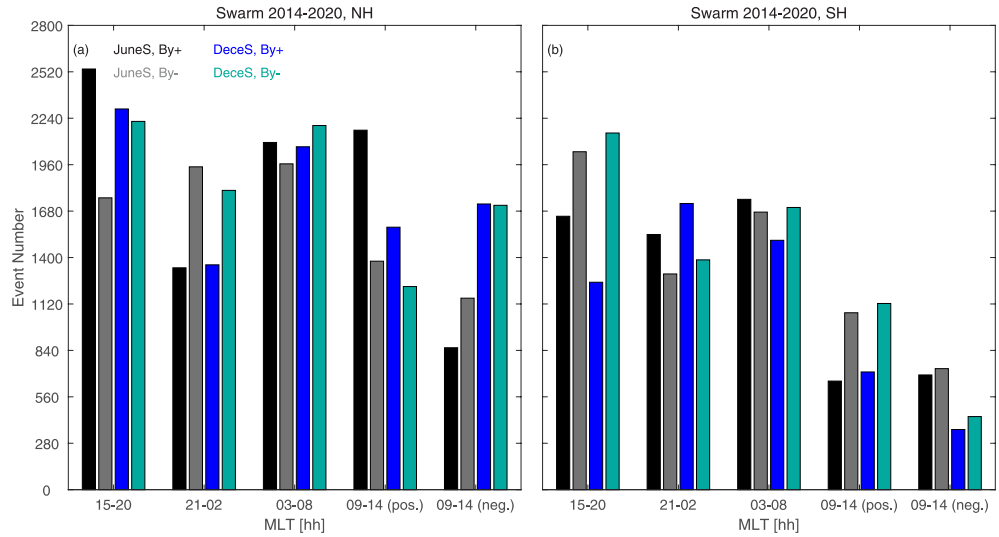

Figure 1. The event number of auroral crossings of Swarm A as a function of MLT. The data is divided into two panels: the left panel corresponds to the Northern Hemisphere, while the right panel represents the Southern Hemisphere. The bars are color-coded to distinguish between different conditions: black bars correspond to June solstice and IMF $B_y > 0$, gray bars correspond to June solstice and IMF $B_y < 0$, blue bars correspond to December solstice and IMF $B_y > 0$, and green bars correspond to December solstice and IMF $B_y < 0$. The MLT sectors are arranged from left to right as follows: 15–20 MLT, 21–02 MLT, 03–08 MLT, and 09–14 MLT. The 09–14 MLT sectors are further differentiated based on the presence of eastward and westward peak polar electrojets (PEJ).

Furthermore, it serves to circumvent the undesired smearing of current profiles that can arise from simplistic averaging techniques.

The resulting latitudinal variation of PEJ and FACs profiles are shown in Figures 2 and 3, distinguishing between IMF $B_y > 0$ and IMF $B_y < 0$. Within these figures, 0°ΔMLat denotes the latitude of the peak PEJ, with positive values indicating latitudes closer to the pole. The figure has a truncation range of ±10° ΔMLat with a bin size of 2° ΔMLat. Each panel features five curves in different colors, each representing a different local time sector. The latitude variations of PEJ and FAC in Figures 2 and 3 are quite similar. The panels in Figures 2a–2d and 3a–3d show the distribution of PEJ, and Figures 2e–2h, 3e–3h show FACs, separately for two seasons and two hemispheres. Notably, the red curves in the panels illustrate the dominance of eastward PEJ in the dusk sector, while the blue and black curves signify westward PEJ in the 21–02 MLT and dawn sectors, respectively. This pattern aligns with the characteristic dual-cell configuration of the polar electrojet, comprising clockwise flow on the dawn side and counterclockwise flow on the dusk side, predominantly occurring within the auroral oval. The orientation of the PEJ, whether eastward (brown curves) or westward (green curves), around 09–14 MLT is contingent upon the sign of IMF B_y. At higher latitudes, we observe PEJ signatures with opposite flow directions, signifying sunward return currents over the polar cap.

At 15–20 MLT there is notable upward FAC on the poleward and downward FAC on the equatorward side of the key latitude. These are typical duskside R1 and R2 FACs, flanking the eastward PEJ. In the 21–02 MLT sector, a downward FAC is observed on the poleward, and an upward FAC on the equatorward side of the westward PEJ. Around 21–02 MLT, the conventional classification of R1 and R2 FACs is less applicable due to the proximity to the Harang discontinuity. Typically, three FAC sheets manifest, with the central upward sheet being the most pronounced. In the 03–08 MLT sector, the typical downward R1 and upward R2 FACs can be observed. In the 09–14 MLT sector, the displayed FACs represent the midday R1 and the R0 in the polar cap. Their directions are controlled by IMF B_y orientation, with the upward (downward) R0 current and downward (upward) R1 FAC related to eastward (westward) DPY ionospheric current. For the sake of clarity, we label FAC on the poleward side of the key latitude as FACp and those on the equatorward side as FACe in the following text. Thus, at dusk and dawn, FACp corresponds to R1 FAC, while FACe corresponds to R2 FAC. In the 09–14 MLT sector, FACp represents midday R0 FAC, and FACe represents midday R1 FAC. Around 21–02 MLT, FACp flows into the ionosphere, while FACe flows out of the ionosphere.

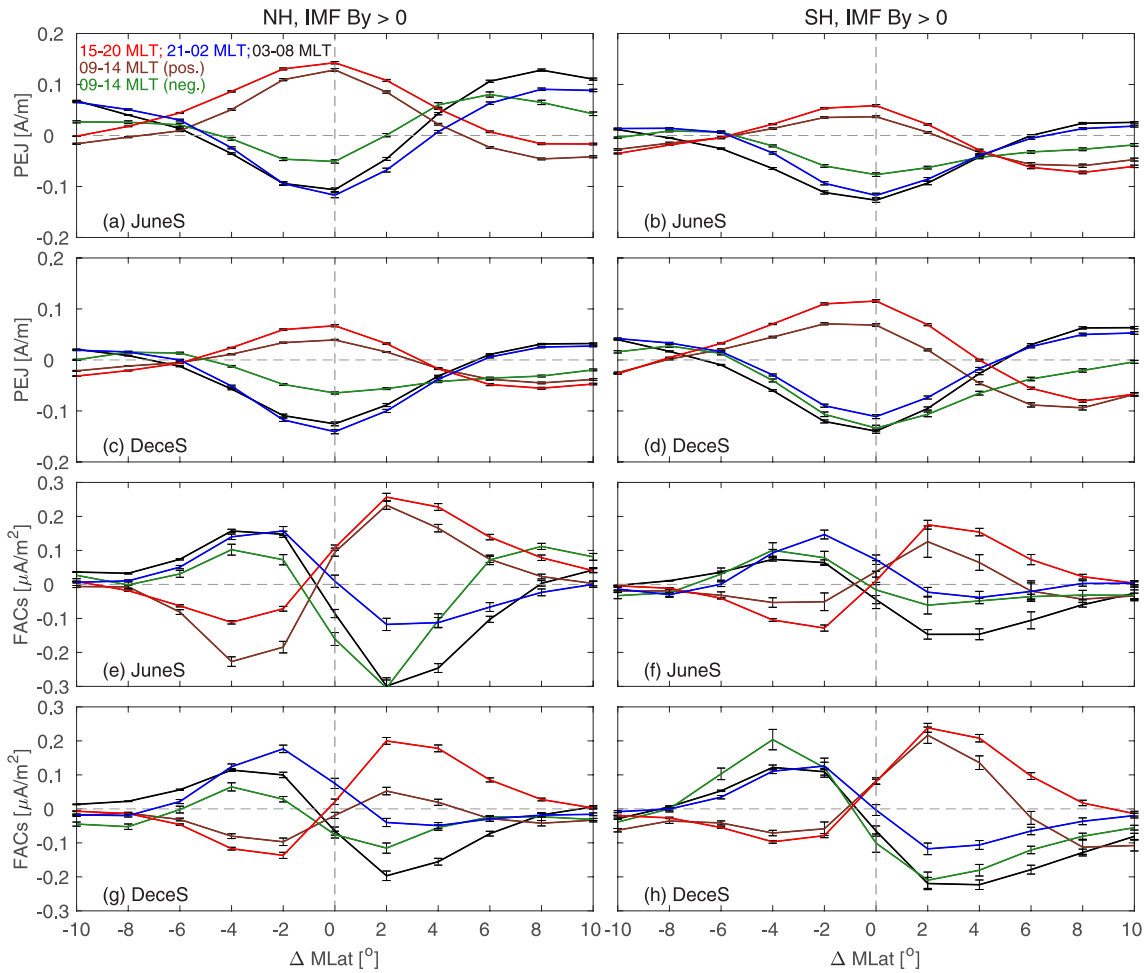

Figure 2. Superposed location analysis of the magnetic latitudinal distribution of PEJ (a-d) and FACs (e–h) for IMF $B_y > 0$ at four local time sectors in the Northern (a, c, e, g) and Southern (b, d, f, h) Hemispheres. The analysis is carried out separately for two solstice periods: June solstice (JuneS, a, b, e, f) and December solstice (DeceS, c, d, g, h). The reference location, marked as 0° ΔMLat, represents where the PEJ attain peaks. Negative ΔMLat denotes regions equatorward of the peak electrojet, and positive ΔMLat denotes regions poleward of the peak electrojet. Vertical gray bars represent the standard deviation of averages.

4. Statistical Results

The absolute peak value of FACp and FACe during JuneS (denoted by asterisks) and DeceS (denoted by circles) for IMF $B_y > 0$ are shown in Figure 4. The blue dashed line represents the Northern Hemisphere and the red dashed line represents the Southern Hemisphere. The panels from left to right correspond to 15–20 MLT, 21–02 MLT, 03–08 MLT, 09–14 MLT sectors, encompassing both positive and negative PEJ. For the sake of comparison with the peak amplitudes of PEJ and FACs, the zonal variations of mean E_m, ionospheric conductance, IMF B_y and B_z are presented in the bottom four panels of Figure 4. The ionospheric Hall conductance due to sunlight (following Moen & Brekke, 1993) is derived for each peak PEJ event. Notably, the average E_m remains below 1.8 mV/m, and the IMF B_z is larger than −1.2 nT, indicating a relatively quiet study period on average. The averaged IMF B_y is around 3 nT in the five MLT sectors.

On the duskside, it is evident that FACp (upward R1 FACs, Figure 4a) exhibit greater strength during local summer compared to local winter, evidenced by the declining trend in the blue line and the rising trend in the red line. This trend is consistent with the overall seasonal variation observed in the ionospheric conductance, which tends to be larger in summer than in winter (Figure 4p). However, the changing trend in ionospheric conductance is not completely consistent with that of FACp. Figure 4a demonstrates that the FACp intensity in local summer and local winter is closer in DeceS, while Figure 4p displays symmetric changes of conductance in JuneS and DeceS. This discrepancy could be attributed to E_m and IMF B_z, which exhibit larger value in winter than in

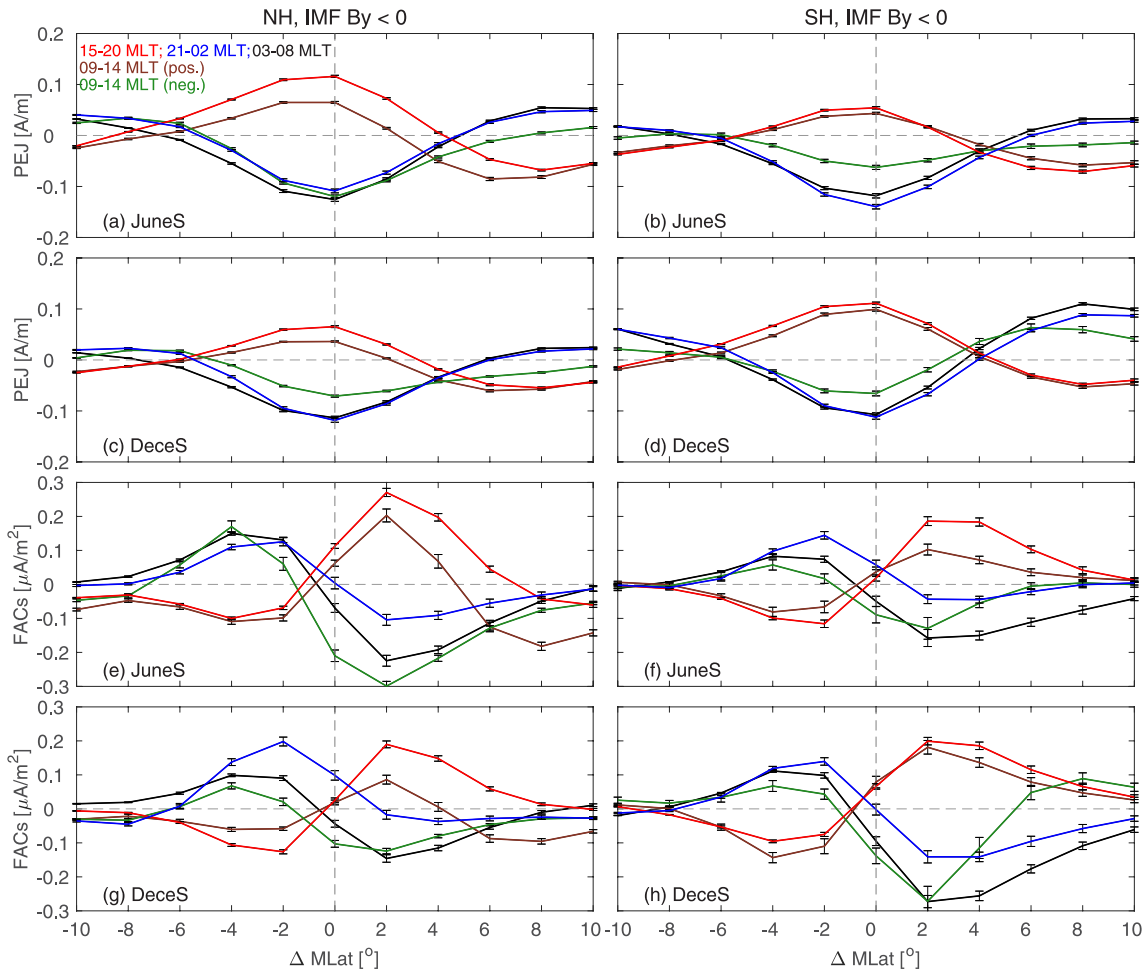

Figure 3. Similar format as Figure 2, but for IMF $B_y < 0$. Superposed location analysis of the magnetic latitudinal distribution of PEJ (a–d) and FACs (e-h) for IMF $B_y < 0$ at four local time sectors in the Northern (a, c, e, g) and Southern (b, d, f, h) Hemispheres. The analysis is carried out separately for two solstice periods: June solstice (JuneS, a, b, e, f) and December solstice (DeceS, c, d, g, h). The reference location, marked as 0° ΔMLat, represents where the PEJ attain peaks. Negative ΔMLat denotes regions equatorward of the peak electrojet, and positive ΔMLat denotes regions poleward of the peak electrojet. Vertical gray bars represent the standard deviation of averages.

summer in both hemispheres, potentially weakening the effect of ionospheric conductance. Moreover, IMF B_y is stronger in winter than in summer in the SH, contradicting the ionospheric conductance effect. These factors might explain the inconsistency in the changing trend between FACp and ionospheric conductance. One can notice that, nevertheless, the FACe (downward R2 FACs, Figure 4f) shows contrasting seasonal variation, which might be linked to the seasonal variation of E_m or B_z (Figure 4k). Another plausible factor contributing to this variation is the seasonal variation of the polar cap Pedersen current (Zhou & Lühr, 2017). During the winter, Pedersen current is relatively weak in the polar region, causing the duskside R1 to largely close by the duskside R2. Conversely in summer, Pedersen currents across the polar cap are stronger, facilitating a more prominent connection between the dusk and dawn side R1 FACs.

At 21–02 MLT, the seasonal change of FACp (downward FACs, Figure 4b) can be generally attributed to the ionospheric conductance effect due to solar illumination (Figure 4q). One can note that FACp shows larger difference in JuneS than in DeceS, although the ionospheric conductance shows greater difference in DeceS than in JuneS (Figure 4q). The ionospheric conductance effect might be compromised by E_m and IMF B_z, as E_m and IMF B_z exhibit weaker difference in DeceS. The relatively minor seasonal variation of FACe (upward FACs, Figure 4g) might be related to the total conductance due to a combination of both solar illumination and particle precipitation. It is worth noting that energetic electron precipitation in the upward FACs region on the nightside tends to be suppressed by sunlight due to the ionospheric feedback effect, as outlined in Newell et al. (1996). This

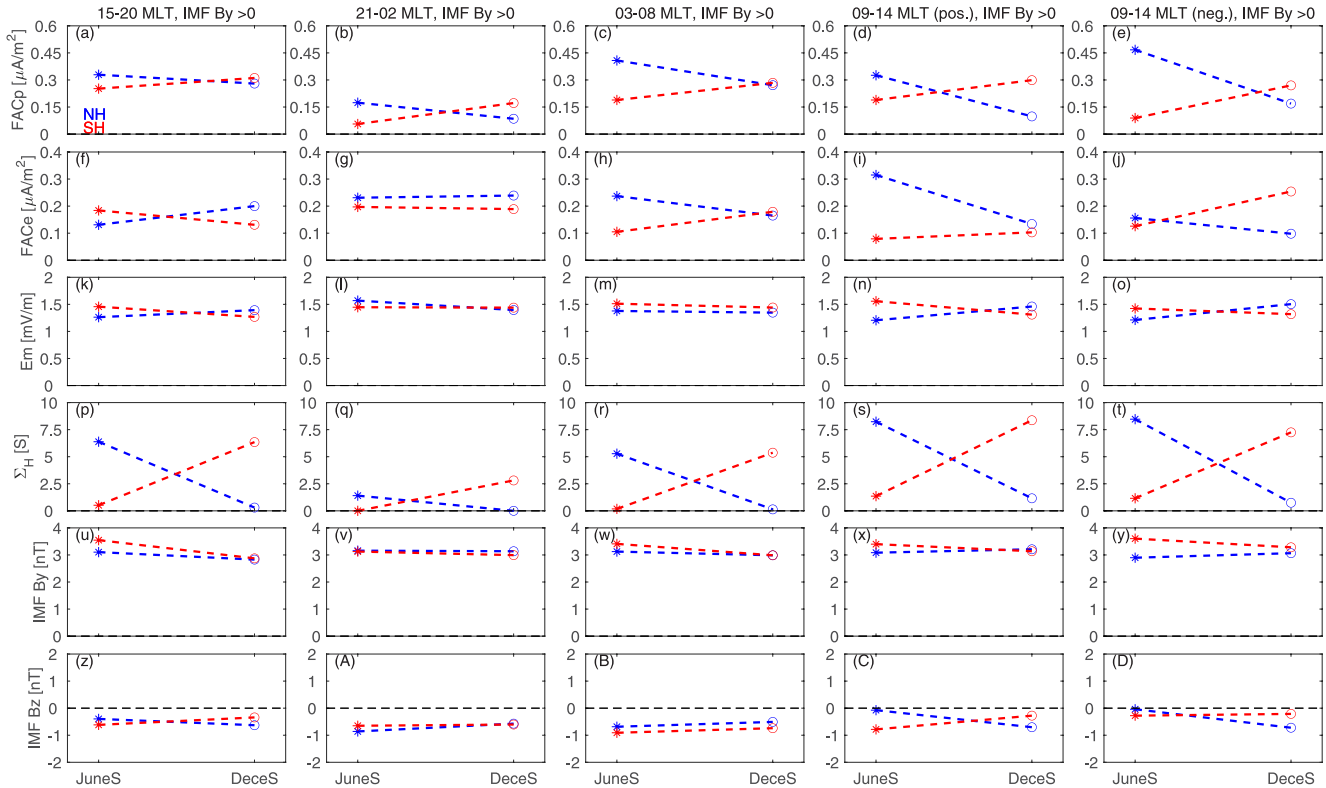

Figure 4. The absolute peak strength of FACp (a–e) and FACe (f–j) when IMF $B_y > 0$. Also shown are E_m (k–o), ionospheric conductance (p–t), IMF B_y (u–y) and B_z (z–D). The data is presented in five columns, each pertaining to different local time sectors: from left to right columns are 15–20 MLT (a, f, k, p, u, z), 21–02 MLT (b, g, l, q, v, A), 03–08 MLT (c, h, m, r, w, B), 09–14 MLT for positive (d, i, n, s, x, C) and negative peak PEJ (e, j, o, t, y, D). The asterisk denotes June solstice, and the circle represents December solstice. To aid in interpretation, blue dashed lines represent Northern Hemisphere data, and red dashed lines represent Southern Hemisphere data.

feedback mechanism likely explains why solar illumination doesn't significantly impact the nightside upward FACs density, a finding consistent with the research of Wang et al. (2005). The downward ΔFACp (Figure 4b) is less affected by electron precipitation, depending more on solar illumination, thus, is stronger in the summer hemisphere with higher conductance.

On the dawnside, the current in both NH and SH is greater in summer than in winter. However, in DeceS, FACe is similar in the NH and SH, while conductance shows a larger value in the SH than in the NH. In the 09–14 MLT sectors, both FACe and FACp are in general stronger in summer compared to winter (Figures 4d, 4e, 4i, 4j), implying the important role of ionospheric conductance. Nonetheless, there are differences in the changing trends of FACs and ionospheric conductance. Such a trend discrepancy might stem from the nearly opposite effect of E_m and ionospheric conductance. Additionally, empirical ionospheric conductance models might deviate from the real situation. Our analysis did not consider the particle precipitation effect, which could also affect the FACs intensity. However, despite this, FACs at dawn and 09–14 MLT in both hemispheres generally exhibit higher intensities in local summer than in winter, indicating the important role of solar-illuminated conductance. Notably, the variations in FACp and FACe in the 09–14 MLT sector are not the same, indicating different sources within the magnetosphere for these two kinds of currents. We will discuss this difference in more details in the discussion section.

The absolute peak values of FACp and FACe in JuneS (indicated by asterisks) and DeceS (indicated by circles) for IMF $B_y < 0$ are presented in Figure 5, in the same format as Figure 4. The average E_m remains below 1.8 mV/m, and the IMF B_z is larger than −1.2 nT, indicating an overall quiet period on average. The averaged IMF B_y is around −3 nT in the five MLT sectors. The seasonal variation for IMF $B_y < 0$ is basically similar to that for IMF $B_y > 0$ except for NH FACe during 21–02 MLT (Figure 5g). In most local times (Figures 5a–5e, 5h–5j), there is a consistent trend of FACs exhibiting greater strength during local summer compared to local winter. For example, the blue dashed line in the NH shows a declining trend from JuneS to DeceS, whereas the red dashed line in the SH

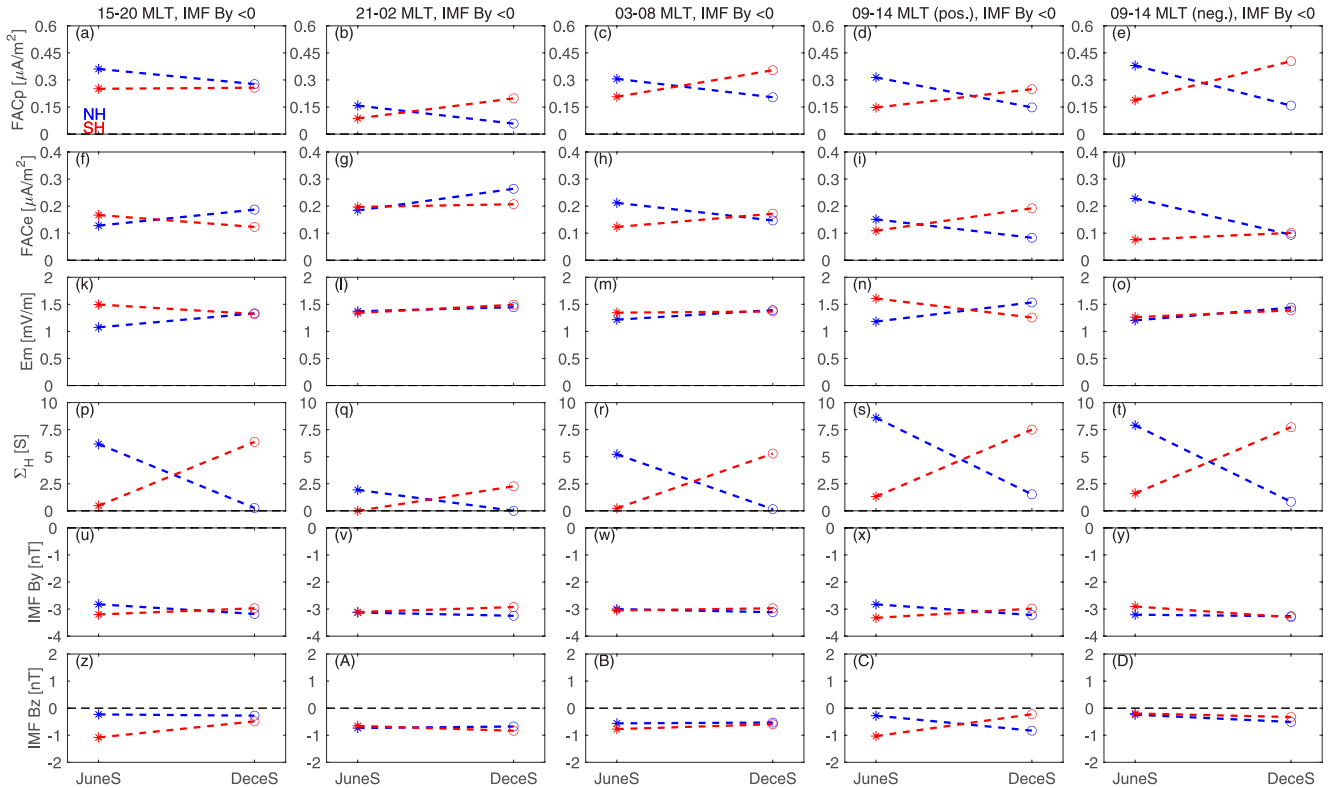

Figure 5. Same format as Figure 4, but for IMF $B_y < 0$. The absolute peak strength of FACp (a–e) and FACe (f–j) when IMF $B_y < 0$. Also shown are E_m (k–o), ionospheric conductance (p–t), IMF B_y (u–y) and B_z (z–D). The data is presented in five columns, each pertaining to different local time sectors: from left to right columns are 15–20 MLT (a, f, k, p, u, z), 21–02 MLT (b, g, l, q, v, A), 03–08 MLT (c, h, m, r, w, B), 09–14 MLT for positive (d, i, n, s, x, C) and negative peak PEJ (e, j, o, t, y, D). The asterisk denotes June solstice, and the circle represents December solstice. To aid in interpretation, blue dashed lines represent Northern Hemisphere data, and red dashed lines represent Southern Hemisphere data.

exhibits an ascending trend. This is consistent with the seasonal variation of the solar-induced ionospheric conductance. The seasonal variation in the duskside FACe (R2 FACs, Figure 5f) closely resembles that of E_m (Figure 5k). Interestingly, the nighttime FACe in the SH (red curve, Figure 5g) displays minimal differences between summer and winter, similar to the pattern observed for IMF $B_y > 0$. However, in the NH, the nighttime FACe (blue curve, Figure 5g) is stronger in winter than in summer, possibly due to the higher particle precipitation during local winter. Similar to the case of IMF $B_y > 0$, there are also differences in the trends of conductance and FACs, indicating the influence of other factors, such as E_m, particle precipitation, and the utilization of empirical solar conductance models.

Figure 6 illustrates the differences in the absolute density of FACs between IMF $B_y > 0$ and IMF $B_y < 0$, denoted as $\Delta\text{FAC} = \text{FAC}_{\text{By+}} - \text{FAC}_{\text{By−}}$. A positive ΔFAC means that FACs are larger for IMF $B_y > 0$ than for IMF $B_y < 0$, while a negative ΔFAC suggests the opposite result. It can be seen that ΔFACs exhibit obvious hemispheric, seasonal and local time differences, which cannot be solely explained by ΔE_m (absolute variation less than 0.25 mV/m), ΔB_z (absolute variation less than 0.5 nT), or ionospheric conductance (absolute variation less than 0.75 S), as demonstrated in the bottom panels of Figure 6.

Instead, they are primarily driven by the orientation of IMF B_y (variation larger than 5.5 nT) highlighting the significant effect of IMF B_y on FACs. In the dusk sector, the NH R1 FACs (ΔFACp, Figure 6a) are larger for IMF $B_y < 0$ than for IMF $B_y > 0$, whereas the SH R1 FACs exhibit the opposite pattern, being stronger for IMF $B_y > 0$ than for IMF $B_y < 0$. This trend is reversed in the dawn sector: NH R1 FACs (Figure 6c) are stronger when IMF $B_y > 0$, while SH R1 FACs are stronger when IMF $B_y < 0$. The IMF B_y effect is more prominent in local summer than in local winter. Around 21–02 MLT, the hemispheric difference in ΔFACp (Figure 6b) follows a similar pattern to that observed in the dawn, albeit with a somewhat less seasonal variation. In the

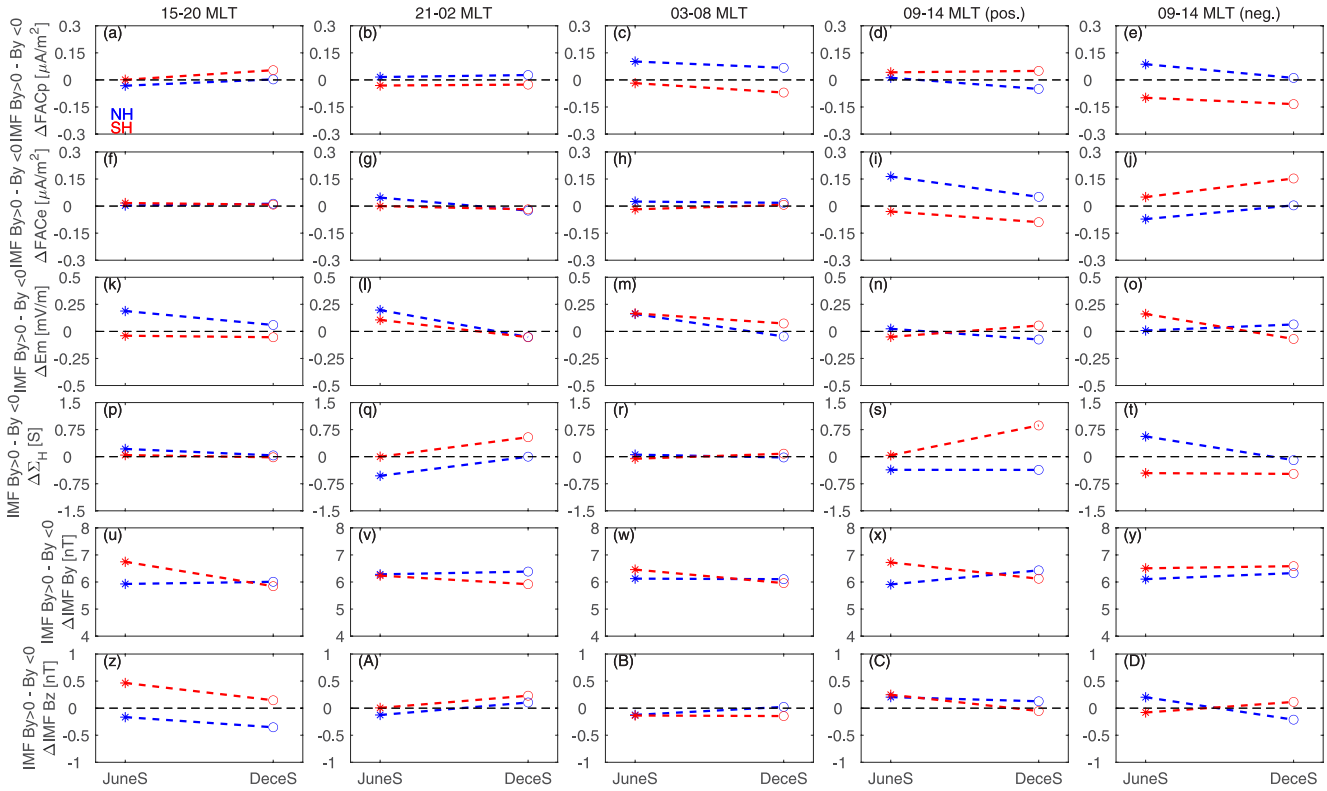

Figure 6. Differences in absolute peak strength of FACp (a–e) and FACe (f–j) between IMF $B_y > 0$ and IMF $B_y < 0$. Also shown are differences in E_m (k–o), ionospheric conductance (p–t), IMF B_y (u–y) and B_z (z–D). The data is presented in five columns, each pertaining to different local time sectors: from left to right columns are 15–20 MLT (a, f, k, p, u, z), 21–02 MLT (b, g, l, q, v, A), 03–08 MLT (c, h, m, r, w, B), 09–14 MLT for positive (d, i, n, s, x, C) and negative peak PEJ (e, j, o, t, y, D). The asterisk denotes June solstice, and the circle represents December solstice. To aid in interpretation, blue dashed lines represent Northern Hemisphere data, and red dashed lines represent Southern Hemisphere data.

dawn, dusk and 21-02 MLT sectors, ΔFACe (Figures 6a–6h) exhibits a lesser dependence on the sign of IMF B_y when compared to ΔFACp.

The situation differs around 09–14 MLT sector, as FACp and FACe display distinct but opposite response to IMF B_y. The NH FACp is larger for IMF $B_y < 0$, while the SH FACp is larger for IMF $B_y > 0$ (09–14 MLT, PEJ positive, Figure 6d). Conversely, the impact of IMF B_y on FACe (Figure 6i) is reversed, with NH FACe being stronger for IMF $B_y > 0$ and SH FACe being larger for IMF $B_y < 0$. When the westward PEJ dominates in 09–14 MLT (PEJ negative, Figures 6e and 6j), the impact of IMF B_y on FACp and FACe precisely reverses compared to when the eastward PEJ dominates. In both eastward and westward PEJ cases, the IMF B_y effect on FACs is more prominent in local summer, except for the stronger NH ΔFACp in winter for IMF $B_y < 0$, which can be attributed to the variation of ΔE_m (Figure 6d).

In summary, in the local time sectors characterized by a prevailing positive PEJ (dusk and 09–14 MLT), the SH exhibits a stronger FACp compared to that of the NH when IMF $B_y > 0$. Conversely, in the MLT sectors dominated by a negative PEJ (dawn, 21–02 MLT, and 09–14 MLT) the IMF B_y sign effect is reversed, meaning that, when IMF $B_y > 0$, the FACp in the Southern Hemisphere surpassed that in the Northern Hemisphere. FACe exhibits a weaker response to IMF B_y at dusk, dawn and 21–02 MLT, but shows a distinct and opposite variation compared to FACp around 09–14 MLT.

The dependence of the FACs' peak magnetic latitude on the polarity of IMF B_y is evident, as illustrated in Figure 7, following the same format as Figure 6. A positive ΔMLat indicates that FACs are found at higher latitudes for IMF $B_y > 0$ than for IMF $B_y < 0$. Both FACp and FACe exhibit similar variations in response to the sign of IMF B_y. At dusk and 09–14 MLT with a positive PEJ (Figures 7a, 7f, 7d, 7i), NH FACs tend to be located at higher latitudes for IMF $B_y > 0$ than for $B_y < 0$, except for dusk in DeceS; while the SH FACs tend to be at higher latitudes for IMF $B_y < 0$ than for IMF $B_y > 0$, except for dusk in JuneS. In the 21–02 MLT, dawn, and

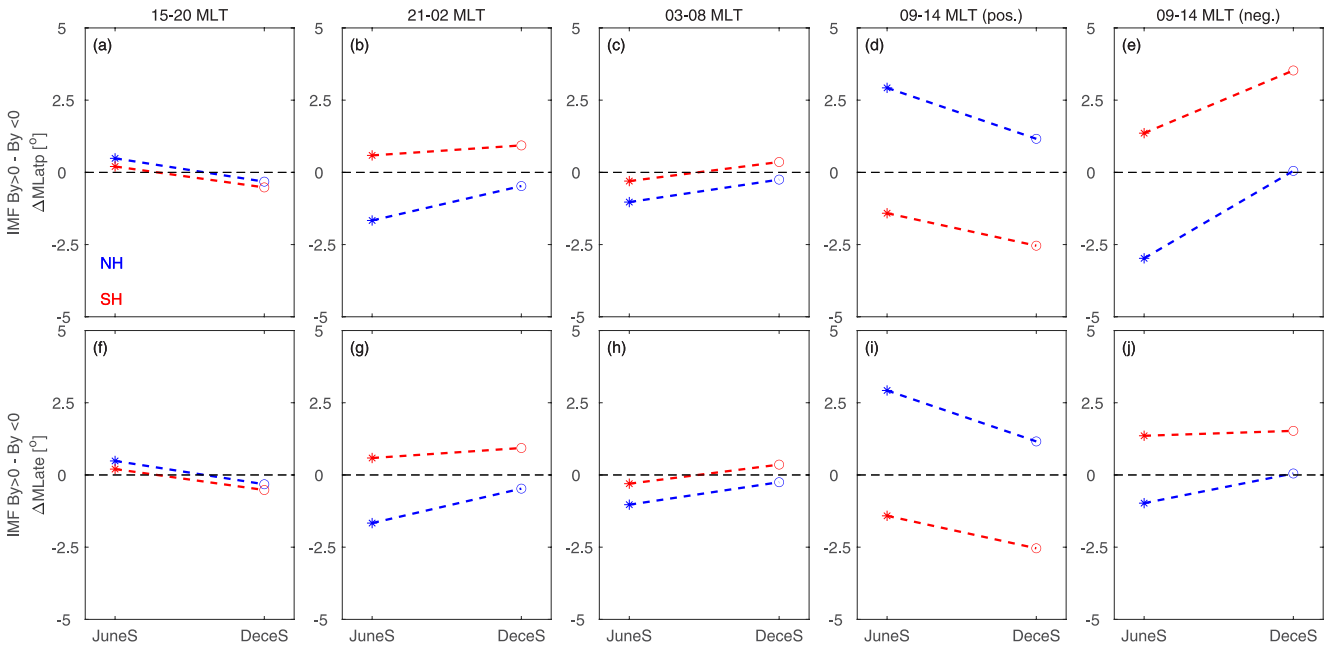

Figure 7. Differences in absolute MLat of FACp (a–e) and FACe (f–j) between conditions of IMF $B_y > 0$ and IMF $B_y < 0$. The data is categorized into five columns. From left to right columns are 15–20 MLT (a, f), 21–02 MLT (b, g), 03–08 MLT (c, h), 09–14 MLT for positive (d, i) and negative peak PEJ (e, j). The asterisk denotes June solstice, and the circle represents December solstice. To aid in interpretation, blue dashed lines signify the Northern Hemisphere, while red dashed lines represent the Southern Hemisphere data.

09–14 MLT sectors with negative PEJ (Figures 7b, 7g, 7c, 7h, 7e, 7j), SH FACs are positioned at higher latitudes for IMF $B_y > 0$ than for IMF $B_y < 0$, except for dawn in JuneS. On the other hand, NH FACs exhibit the opposite variation, that is, they are located at higher latitudes for IMF $B_y < 0$ than for IMF $B_y > 0$. This specific IMF B_y effect is more prominent in local summer than in local winter. It's worth noting that, when comparing IMF $B_y > 0$ to IMF $B_y < 0$, FACs are located at higher latitudes in JuneS than DeceS at dawn and 09–14 MLT with eastward PEJ. Conversely, in DeceS, FACs are at higher latitude than in JuneS at dusk, 21–02 MLT and 09–14 MLT with westward PEJ.

5. Discussion

In this study, we investigate the impact of IMF B_y on the peak current density and location of FACs using data from the dual satellite pair, Swarm A and C, spanning the period from 2014 to 2020, which encompasses 6 years. It demonstrates that the IMF B_y has a significant impact on the peak strength and latitude of FACs, exhibiting significant local time, seasonal and hemispheric differences.

We made use of the IMF data at the bow shock. From those we calculated our IMF B_y by averaging the values between 10 and 20 min before the observed peak in PEJ. Vennerstrom et al. (2005) considered an average delay of 15 min for the development of the FACs from the magnetopause to the response at the ionosphere. Laundal et al. (2018) used the solar wind and IMF parameters averaged over the 20 min preceding the corresponding Swarm/CHAMP measurements. Holappa et al. (2023) and Kubyshkina et al. (2023) adopted 1 hr averaged IMF components spanning from 1981 to 2019 to investigate the IMF B_x effect on AL index. To investigate the effect of delay times on the influence of IMF B_y on FACs, we changed the time window size in 10-min intervals from 10 min up to 1 hr. This involved averaging IMF B_y values from different time spans: 0–10 min, 0–20 min, 0–30 min, 0–40 min, 0–50 min, 0–60 min before the peak PEJ detection. Figure S2 in Supporting Information S1 supplementary file shows the differences in absolute peak strength of FACp (a–e) and FACe (f–j), as well as the absolute MLat of FACp (k–o) and FACe (p–t) between IMF $B_y > 0$ and IMF $B_y < 0$, considering the various time delays. Notably, these diverse averaging time window sizes do not alter the conclusions drawn from the analysis significantly.

5.1. Local Time Effect of IMF B_y on FACs Density

In the dusk and 09–14 MLT sectors, characterized by the prevalence of eastward PEJ, NH FACp are stronger when IMF $B_y < 0$ than when IMF $B_y > 0$. On the contrary, at dawn, 21-02 MLT, and 09–14 MLT dominated by westward PEJ, NH FACp are stronger when IMF B_y is positive than when it is negative. In contrast, the SH FACp shows reverse dependences on the IMF B_y orientation. As for FACe, their response to IMF $B_y < 0$ is similar to that of FACp at dawn, dusk and 21–02 MLT, albeit with a lesser degree of variation. This discrepancy might be due to the different source regions of R1 and R2 FACs. R1 FACs originate from the magnetopause, rendering them more directly influenced by solar wind and IMF. On the other hand, R2 FACs originate from the inner magnetosphere, making them less susceptible to IMF B_y. This distinction potentially accounts for the relatively weaker dependence of FACe at dawn, dusk and 21–02 MLT on the orientation of IMF B_y.

Nevertheless, when it comes to the midday R1 FACs (FACe), their behavior shows obvious variation with the polarity of IMF B_y, and this dependence is opposite to that of midday R0 FACs (FACp). In the NH, at 09–14 MLT with eastward PEJ FACe are stronger when IMF $B_y > 0$, while NH FACe are stronger when IMF $B_y < 0$ with westward PEJ. Conversely, the IMF B_y effect on the SH FACe is reversed in polarity. McDiarmid et al. (1979) proposed that the midday R1 currents correspond to R1 currents that extend from the dawn (IMF $B_y > 0$) and dusk (IMF $B_y < 0$) hours in the NH, while from the dusk (IMF $B_y > 0$) and dawn (IMF $B_y < 0$) in the SH. However, our findings indicate that the midday R1 FACs (associated with eastward PEJ) shares similar features with the dawnside R1 FACs, while the midday R1 FACs (related to westward PEJ) resemble R1 FACs in the dusk sector. This pattern holds true for both Northern and Southern Hemispheres, contradicting the speculation by McDiarmid et al. (1979). Our observations suggest that the midday R1 current is not simply an extension of R1 current from the dawn and dusk side, thus supporting the result of Taguchi et al. (1993). Using the magnetic field and electron data from DE 2 satellite, Taguchi et al. (1993) advocated a model wherein both midday R1 and R0 FACs reside on open geomagnetic field lines and are different from the R1/R2 current systems in the dawn and dusk sectors that are located primarily on closed geomagnetic field lines. Yamauchi et al. (1993) proposed nearly a similar concept to Taguchi et al. (1993), except that the source of the closed magnetic field line region also contributes to the midday R1 FACs.

Interestingly, the IMF B_y effect on midday R1 FACs (FACe) seems to be consistent with the statistical patterns of midday PEJ. When IMF B_y is dawnward (duskward), it tends to favor the development of westward PEJ in the Northern Hemisphere (Southern Hemisphere), consistent with the statistically significant response of DPY current to the polarity of IMF B_y. During periods of duskward (dawnward) IMF B_y, the DPY current in the NH primarily flows eastward (westward), while this effect is reversed in the SH (e.g., Friis-Christensen & Wilhjelm, 1975; Vennerstrom et al., 2002). Consequently, the NH eastward (westward) PEJ is stronger when IMF $B_y > 0$ (IMF $B_y < 0$), while the SH eastward (westward) PEJ is stronger when IMF $B_y < 0$ ($B_y > 0$). This B_y effect on PEJ is more pronounced in the summer hemisphere, where ionospheric conductance is higher (figure not shown). The response of midday FACe mirrors that of the PEJ, suggesting a closer connection between the equatorward-side FACs (midday R1 FACs) and PEJ. One can notice that the dependence of midday R0 FACs (FACp) on the polarity of IMF B_y is opposite to that of midday R1 FACs, indicating different source mechanisms for midday R0 and R1 currents. Midday R0 FACs originate from open field line regions, whereas midday R1 FACs can exist in both open and closed field line regions (e.g., Wang et al., 2008).

Our work shows that strongly positive IMF B_y seems to enhance the dawn FACs, which is consistent with the previous work of Holappa et al. (2021) based on the constellation of polar-orbiting commercial Iridium satellites in 2010–2017. They observed that FACs in the dawn sector are significantly stronger for IMF $B_y > 0$ than for IMF $B_y < 0$ in the NH winter, and for IMF $B_y < 0$ than for IMF $B_y > 0$ in the SH winter. However, their studies reported that the dependence of FACs in the dusk sector on IMF B_y was less pronounced. In contrast, our study reveals that R1 FACs on the duskside exhibit a prominent but reversed dependence on the IMF B_y sign compared to the dawnside FACs. This discrepancy between our findings and those of Holappa et al. (2021) may stem from the utilization of different satellite data sources. Furthermore, our results on the duskside FACs are consistent with the work of Hu et al. (2014), who noted that the afternoon aurora intensity in the Southern Hemisphere is stronger when IMF B_y is greater than zero, while in the Northern Hemisphere, it is stronger when IMF B_y is less than zero. Given the close correlation between upward FACs and auroral electron precipitation flux, it's plausible that the IMF B_y polarity dependence observed in the upward R1 FACs on the duskside mirrors the variations in aurora intensity, as previously demonstrated by Hu et al. (2014).

5.2. Seasonal Dependence of IMF B_y Effect

Previous research has indicated that the influence of IMF B_y on auroral activity, as measured by the AL index, is more pronounced in the winter hemisphere than in the summer hemisphere. Holappa and Mursula (2018) reported that in the NH winter, the AL index was 40%–50% higher for IMF $B_y > 0$ compared to IMF $B_y < 0$, whereas in the NH summer, the AL index was only about 10% stronger for IMF $B_y < 0$ than for IMF $B_y > 0$. A similar pattern was observed in the SH, with a clearly reversed IMF B_y effect in winter and a weak IMF B_y effect in summer. This observed seasonal disparity for the impact of IMF B_y may be attributed to the ionospheric conductance, which is predominantly induced by particle precipitation in local winter. Particle precipitation exhibits explicit IMF B_y dependence according to Holappa et al. (2020). This might clarify why the IMF B_y influence on geomagnetic activity tends to be more substantial in local winter, compared to local summer.

In contrast to the winter preference of the IMF B_y effect, there are studies indicating that the IMF B_y effect is nearly equal in both summer and winter hemispheres. Reistad et al. (2020) revealed that IMF B_y controls the dayside reconnection rate, which governed the global energy input into the magnetosphere. Consequently, the effect of IMF B_y on auroral currents is found to be equally strong in the summer and winter hemispheres. Similarly, Holappa et al. (2020) demonstrated that the IMF B_y dependence of diffuse electron precipitation, occurring at dawn and 21–02 MLT, exhibits roughly the same level of strength in both the winter and summer hemispheres. These findings suggest that, in certain cases, the influence of IMF B_y on geomagnetic phenomena may not exhibit a significant seasonal preference and can be equally pronounced across hemispheres.

Our work reveals that the IMF B_y effect on FACs strength is more significant in the summer hemisphere in most local time sectors, except during 21–02 MLT. This observation indicates that the impact of IMF B_y is more significant in regions characterized by larger conductance. A previous study by Laundal and Østgaard (2009) proposed the existence of inter-hemispheric FACs (IHFACs) that flows upwards at dusk and downward at dawn in the dark SH. This phenomenon was attributed to differences in ionospheric conductance between the summer and winter hemispheres. Conversely, Lyatskaya et al. (2014) suggested that in the summer hemisphere, IHFACs and R1 FACs share the same direction, while in the winter hemisphere, they flow in opposite directions. This finding aligns with the observed seasonal variation of FACs in response to IMF B_y in our study, where the magnitude of FACp in the dark winter hemisphere is less than that in the sunlit hemisphere. These results support the notion that IMF B_y can have a significant influence on FACs, especially in regions with high ionospheric conductance.

5.3. Hemispheric Difference of IMF B_y Effect

Interestingly, our work shows that in regions where eastward PEJ dominates (dusk and 09–14 MLT with positive PEJ), the SH FACp are stronger than its NH counterpart when comparing IMF $B_y > 0$ to IMF $B_y < 0$. Conversely, in regions characterized by westward PEJ dominance (dawn, 21–02 MLT, and 09–14 MLT with negative PEJ), NH FACp are stronger than SH FACp in the case of positive IMF B_y. This observation highlights the dynamic interaction between IMF B_y polarity, local time sector, and hemispheric difference in the strength of FACp.

To illustrate the impact of IMF B_y on the hemispheric differences in FACp strength, Figure 8 provides a schematic representation of FACs in the two hemispheres for IMF $B_y < 0$ (left panel) and IMF $B_y > 0$ (right panel). On the left side, it shows the duskside with westward PEJ, while the right side depicts the dawnside with eastward PEJ. In this representation, R1 FACs on the poleward side of the eastward (westward) PEJ typically flow into (out of) the ionosphere.

For a more negative IMF B_y, there are IHFACs flowing on the dawn and dusk sides from the NH into the SH. As a result, R1 FACs are a combination of two FAC components: one originating from the magnetopause and the other flowing between conjugate ionospheres. Consequently, the SH FACp on the dawnside and NH FACs on the duskside are strengthened because IHFACs are in the same direction as R1 FACs. On the contrary, NH FACp on the dawnside and SH FACs on the duskside are weakened because IHFACs oppose R1 FACs.

For a more positive IMF B_y, IHFACs are suggested to flow from the SH into the NH. Consequently, the SH FACp on the duskside and NH FACs on the dawnside are strengthened, while the NH FACp on the duskside and SH FACs on the dawnside are weakened. Thus, the IHFACs induced by IMF B_y can explain the larger SH FACp for IMF $B_y > 0$ than for IMF $B_y < 0$, and the larger NH FACp for IMF $B_y < 0$ than for IMF $B_y > 0$ in the dusk and

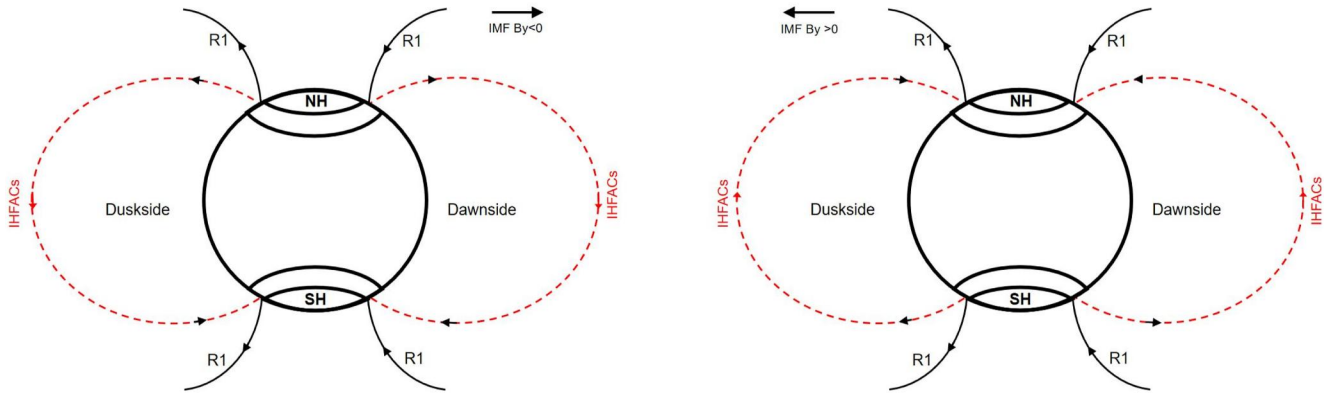

Figure 8. Schematic diagram of FACs and interhemispheric FACs (IHFACs) under two different conditions for IMF $B_y < 0$ (dawnward, left panel) and IMF $B_y > 0$ (duskward, right panel). IHFACs flow from the Southern Hemisphere to the Northern Hemisphere for IMF $B_y < 0$ and vice versa for IMF $B_y > 0$ (represented by red dashed line with black arrow). Black lines with arrows indicate R1 FACs. The left side of the diagram represents the dusk sector, which corresponds to dusk and 09–14 MLT sectors dominated by eastward PEJ, and the right side of the diagram represents the dawn sector, encompassing 21–02 MLT, dawn, and 09–14 MLT sectors characterized by westward PEJ.

09–14 MLT sectors with eastward PEJ. Conversely, the reverse occurs at dawn, 21–02 MLT and 09–14 MLT with westward PEJ.

This form of IHFACs induced by IMF B_y has been theorized by Stenbaek-Nielsen and Otto (1997). They proposed the existence of an extra B_y component in the magnetotail associated with the IMF B_y penetration, exhibiting a radial gradient pointing toward the magnetotail. The non-uniform distribution of this IMF B_y component within the inner magnetosphere could drive IHFACs to flow from the SH into the NH when IMF $B_y > 0$, and vice versa when IMF $B_y < 0$. Hu et al. (2014) observed that the afternoon aurora intensity was brighter for IMF $B_y < 0$ (>0) in the NH (SH). They attributed this to IHFACs flowing from the NH to SH for IMF $B_y < 0$ and conversely for positive IMF $B_y > 0$. Similarly, Liou and Mitchell (2019) reported that the nighttime aurora in the NH tended to be stronger for negative IMF B_y when compared to positive IMF B_y, while at nighttime SH, a brighter aurora was observed for IMF $B_y > 0$ than for IMF $B_y < 0$. This was explained by IHFACs flowing from NH to SH for negative IMF B_y and from SH to NH for positive IMF B_y.

5.4. IMF B_y Effect on the MLat of Peak FACs

Reistad et al. (2020) noted that when IMF B_y and the dipole tilt angle have opposite signs, the polar cap is larger due to larger merging efficiency at the magnetopause. This scenario is applicable to the dusk and 09–14 MLT sectors characterized by eastward PEJ. Specifically, in regions associated with eastward PEJ region during DeceS (when dipole tilt angle is <0), a more positive IMF B_y appears to shift FACs to lower latitudes, when compared to the same region during JuneS. This observation holds true for both the Northern Hemisphere and Southern Hemisphere. However, it's important to note that the findings of Reistad et al. (2020) do not extend to the local time sector dominated by westward PEJ.

In our study, within the region dominated by eastward PEJ (15–21 MLT and 09–14 MLT with positive PEJ), NH FACs tend to reside at higher latitudes than SH FACs when IMF B_y is more positive. Conversely, in the region dominated by westward PEJ (21–02 MLT, 03–08 MLT, and 09–14 MLT with negative PEJ), the situation is reversed: NH FACs are found at lower latitudes compared to SH FACs for a more positive IMF B_y. This pattern holds true for both June solstice and December solstice seasons. Holappa et al. (2021) also reported a similar trend, with the dawnside NH R2 FACs latitudes being about 1°–2° lower for IMF $B_y > 0$ compared to IMF $B_y < 0$, while their study did not addressed latitudes at other local times.

It's worth noting that there is an opposite relationship between the hemispheric difference in the position of FACs and the intensity of FACs. Specifically, stronger FACs tend to be located at lower latitudes, while weaker FACs are positioned at higher latitudes. It can be seen from Figure 8 that during dawn (representing the local time sector with westward PEJ) and IMF $B_y < 0$, the flow direction of IHFAC in the Southern Hemisphere aligns with that of R1 FACs, which might result in an enhancement of the lower latitude segment of R1 FACs. Consequently, this

leads to a shift of the peak R1 FAC toward lower latitudes. Conversely, in the Northern Hemisphere, the flow direction of IHFAC opposes that of R1 FACs, causing a weakening of the lower latitude portion of R1 FACs and a shift in the peak R1 FAC toward higher latitudes.

On the dusk side (representing the local time sector with eastward PEJ) and for IMF $B_y > 0$, the flow direction of IHFAC in the Southern Hemisphere aligns with R1 FACs, reinforcing the equatorward segment of R1 FACs. This can lead to a potential shift in the peak R1 FAC toward lower latitudes. In contrast, in the Northern Hemisphere, the flow direction of IHFACs oppose that of R1 FACs, tending to weaken the lower latitude portion of R1 FACs and potentially causing the peak strength to shift toward higher latitudes. The latitudinal variation of R2 FACs exhibits a comparable pattern with that of R1 FACs and the auroral oval.

One might think that under different magnetic conditions, the above statistical results might be different. Ritter et al. (2004) found the merging electric field, E_m, was a suitable geoeffective solar wind parameter for auroral current intensity. Following their work, we adopted E_m as the activity indicator, with $E_m \leq 2$ mV/m for normal and $E_m > 2$ mV/m for disturbed conditions. Our analysis divided events into two categories: $E_m \leq 2$ mV/m and $E_m > 2$ mV/m, and studied the IMF B_y effect on FACs, as shown in Figures S3 and S4 in Supporting Information S1 files. Comparing the results from the original manuscript with those from magnetic quiet periods reveals similarities, suggesting that when averaging across a large number of events, the impact of less frequent occurrences like magnetic storms and substorms might be masked by the prevalence of quiet period events.

The orientation of IMF Bz component affects the reconnection region between the IMF and Earth's magnetosphere. When IMF $B_z < 0$, it facilitates magnetic reconnection at the dayside magnetopause, while IMF $B_z > 0$ fosters magnetic reconnection at the magnetotail lobe region. This variance could affect the distribution and density of FACs. We specifically conducted examinations of IMF B_y effects under both northward and southward IMF B_z conditions. Figure S5 in Supporting Information S1 file illustrates the differences in FACs intensity and location in different MLT sectors between IMF $B_y > 0$ and IMF $B_y < 0$. In the NH and SH, dark blue and dark red lines represent southward IMF condition, while cyan and orange lines represent northward IMF conditions. Notably, the scenario during IMF $B_z < 0$ is more similar to our work's main results compared to when IMF $B_z > 0$. Despite differences in FACs intensity and latitudes under northward and southward IMF B_z conditions, our paper's main findings remain consistent across these two IMF scenarios. This result is expected, given the higher frequency of quiet-time events during our study period, thus, the polarity of B_z does not alter our conclusions.

The above results are in terms of B_y directions (i.e., IMF $B_y > 0$ and IMF $B_y < 0$). We have also presented results based on the magnitudes of IMF B_y and B_z. Figure S6 in Supporting Information S1 file show the distribution of event numbers as a function of IMF B_y within three ranges of IMF B_z: -4 nT $< B_z < -2$ nT, -2 nT $< B_z < 0$ nT, and 0 nT $< B_z < 2$ nT, each indicated by different colors. Notably, due to the substantial displacement between the geomagnetic and geographic axes in the Southern Hemisphere, there's a relatively lower event number recorded there. Moreover, when IMF Bz exceeds 2 nT or falls below -4 nT, the event number isn't substantial enough to merit consideration within specific local time bins.

Figures S7 and S8 in Supporting Information S1 show the variation of ΔFACp and ΔMLatp with respect to IMF B_y. The red, blue and black curves denote conditions of -4 nT $< B_z < -2$ nT, -2 nT $< B_z < 0$ nT, 0 nT $< B_z < 2$ nT. ΔFACp and ΔMLatp mean that the average value within the respective range of IMF B_z has been subtracted. For conditions -2 nT $< B_z < 0$ and 0 nT $< B_z < 2$ nT, the relationship between ΔFACp, ΔMLatp and IMF B_y is in general consistent with the above conclusions. When the eastward PEJ prevails at dusk and 09–14 MLT, the northern FACp are stronger for more negative IMF B_y than for more positive IMF B_y. Conversely, at dawn, 21–02 MLT, and 09–14 MLT with westward PEJ, the northern FACp are stronger for more positive IMF B_y compared to more negative IMF B_y. The southern FACp generally displays a reversed relationship with IMF B_y direction. A more pronounced IMF B_y effect is observed in local summer in most of local times. The northern FACs are located at higher latitude for more positive IMF B_y than for more negative IMF B_y in local times with eastward PEJ, while the opposite trend is observed in other local times and in the Southern Hemisphere. However, there are deviations in certain situations, such as in the 21–02 MLT in the SH for IMF $B_z < -2$ nT. Figure S6 in Supporting Information S1 highlights a noteworthy decline in the number of events within each category after sorting by the magnitudes of IMF B_y and B_z, with some falling below 100 events. This reduction suggests that specific individual events like substorms or magnetic storms might impact the statistical results.

The hemispheric differences might also arise from the hemispheric asymmetry in magnetic field strengths. Differences in magnetic field strength impact ionospheric conductance by influencing ionospheric plasma (Cnossen et al., 2012) and the particle mirror height, subsequently changing the particle precipitation fluxes (Stenbaek-Nielsen et al., 1973). Figure S9 in Supporting Information S1 file shows the difference in magnetic field strength calculated from the IGRF model between IMF $B_y > 0$ and $B_y < 0$ in five local time sectors. ΔB values are mostly less than zero in nearly all local times in both NH and SH. This might not explain the opposite trend in current changes between the two hemispheres.

Last but not the least, the present work mainly concentrates on the effect of the IMF B_y sign on FACs at June and December solstices, motivated by two nearly opposite viewpoints on solstice. Reistad et al. (2020) showed that the magnetic activity intensified when IMF B_y and dipole tilt angle (DPT) had opposite signs, that is, for IMF $B_y > 0$ and a negative DPT (NH winter) or IMF $B_y < 0$ and a positive DPT (NH summer). This infers that the IMF B_y sign effect is equally strong in both summer and winter hemispheres. In contrast to this perspective, an IMF B_y effect on the auroral westward electrojet, represented by the auroral AL index, was reported to be most prominent during NH winter (Holappa et al., 2021; Holappa & Mursula, 2018). We have noticed that Zhao and Zong (2012) reported that near spring equinox, geomagnetic activity was larger when IMF B_y was negative than when it was positive. In the fall, the situation reversed. They explained the annual variation by correlation between B_y and geomagnetic activity as an aspect of the more fundamental Russell-McPherron effect (Russell & McPherron, 1973). This is an interesting topic that may be worth to be investigated in the future.

6. Summary

In this study, we have comprehensively investigated the influence of the interplanetary magnetic field component, IMF B_y, on the peak current density and location of field-aligned currents (FACs). Data from the dual-satellite pair, Swarm A-C, spanning 6 years, from 2014 to 2020, have been examined. Our research reveals that the polarity of IMF B_y on average significantly impacts the peak current density and location of FACs, demonstrating pronounced local time, seasonal, and hemispheric variations. Specifically, our main findings are summarized in the following:

1. When IMF B_y is positive, the Southern Hemisphere exhibits stronger FACp (poleward side FACs) compared to the Northern Hemisphere, while when IMF B_y is negative, the Northern Hemisphere FACp is stronger than in the Southern Hemisphere. This phenomenon is particularly pronounced in the dusk and 09–14 local time sectors.
2. In local time sectors dominated by westward polar electrojet (PEJ), that is, at dawn, 21–02 MLT, and 09–14 MLT, the Northern Hemisphere FACp is stronger when IMF B_y is positive and weaker when IMF B_y is negative, while the Southern Hemisphere shows the opposite trend.
3. FACe (equatorward side FACs) displays a weaker response to IMF B_y compared to FACp at dawn, dusk and 21–02 MLT, but its variation around 09–14 MLT is opposite to that of FACp.
4. IMF B_y effects on FACs exhibit pronounced seasonal variations, with greater impact observed in local summer than in local winter hemispheres due to ionospheric conductance effects.
5. In the dusk and 09–14 MLT local time sectors, NH FACs tend to reside at higher latitudes than SH FACs when IMF B_y is more positive. Conversely, in local time sectors dominated by westward polar electrojet (PEJ), that is, at dawn, 21–02 MLT, and 09–14 MLT, the situation is reversed: NH FACs are observed at lower latitudes compared to SH FACs for a more positive IMF B_y.
6. There is an opposite relationship between the hemispheric difference in the position of FACs and the intensity of FACs. Specifically, stronger FACs tend to be located at lower latitudes, while weaker FACs are positioned at higher latitudes.

Interhemispheric FACs (IHFACs), flowing from the Southern Hemisphere to the Northern Hemisphere (IMF $B_y < 0$) or vice versa (IMF $B_y > 0$), are introduced to account for the variations in FACp strength and position between the Northern and Southern Hemispheres.

This work provides compelling evidence, based on satellite observations, that IMF B_y significantly influences the strength and location of FACs. Future research endeavors may employ three-dimensional model simulations to enhance our understanding of how IMF B_y affects the coupling system between the magnetosphere and ionosphere.

Data Availability Statement

The Swarm line model PEJ data are from the website https://swarm-diss.eo.esa.int/#swarm%2FLevel2daily%2FLatest _baselines%2FAEJ%2FLPL. The solar wind and interplanetary magnetic field and magnetic activity index data are from NASA/GSFC'S Space Physics Data Facility's OMNIWeb (https://omniweb.gsfc.nasa.gov).

Acknowledgments
The authors greatly appreciate the web availability of data. The authors are grateful for the support from National key research and development program (2022YFF0503700), National Natural Science Foundation of China (42374200), and National Natural Science Foundation of China Basic Science Center (42188101).

References

Aakjær, C. D., Olsen, N., & Finlay, C. C. (2016). Determining polar ionospheric electrojet currents from Swarm satellite constellation magnetic data. *Earth Planets and Space*, *68*(1), 140. https://doi.org/10.1186/S40623-016-0509-Y

Cheng, Z. W., Shi, J. K., Zhang, J. C., Torkar, K., Kistler, L. M., Dunlop, M., et al. (2018). Influence of the IMF cone angle on invariant latitudes of polar region footprints of FACs in the magnetotail: Cluster observation. *Journal of Geophysical Research: Space Physics*, *123*(4), 2588–2597. https://doi.org/10.1002/2017JA024941

Clauer, C. R., & Friis-Christensen, E. (1988). High-latitude dayside electric fields and currents during strong northward interplanetary magnetic field: Observations and model simulation. *Journal of Geophysical Research*, *93*(A4), 2749–2757. https://doi.org/10.1029/ja093ia04p02749

Cnossen, I., Richmond, A. D., & Wiltberger, M. (2012). The dependence of the coupled magnetosphere-ionosphere-thermosphere system on the Earth's magnetic dipole moment. *Journal of Geophysical Research*, *117*(A5), A05302. https://doi.org/10.1029/2012JA017555

Emmert, J. T., Richmond, A. D., & Drob, D. P. (2010). A computationally compact representation of Magnetic-Apex and Quasi-Dipole coordinates with smooth base vectors. *Journal of Geophysical Research*, *115*(A8), A08322. https://doi.org/10.1029/2010JA015326

Erlandson, R. E., Zanetti, L. J., Potemra, T. A., Bythrow, P. F., & Lundin, R. (1988). IMF By dependence of region 1 Birkeland currents near noon. *Journal of Geophysical Research*, *93*(A9), 9804–9814. https://doi.org/10.1029/ja093ia09p09804

Friis-Christensen, E., Finlay, C. C., Hesse, M., & Laundal, K. M. (2017). Magnetic field perturbations from currents in the dark polar regions during quiet geomagnetic conditions. *Space Science Reviews*, *206*(1–4), 281–297. https://doi.org/10.1007/s11214-017-0332-1

Friis-Christensen, E., Kamide, Y., Richmond, A. D., & Matsushita, S. (1985). Interplanetary magnetic field control of high-latitude electric fields and currents determined from Greenland magnetometer data. *Journal of Geophysical Research*, *90*(A2), 1325–1338. https://doi.org/10.1029/JA090iA02p01325

Friis-Christensen, E., & Wilhjelm, J. (1975). Polar cap currents for different directions of the interplanetary magnetic field in the Y-Z plane. *Journal of Geophysical Research*, *80*(10), 1248–1260. https://doi.org/10.1029/JA080i010p01248

Holappa, L., Asikainen, T., & Mursula, K. (2020). Explicit IMF dependence in geomagnetic activity: Modulation of precipitating electrons. *Geophysical Research Letters*, *47*(4), e2019GL086676. https://doi.org/10.1029/2019GL086676

Holappa, L., & Buzulukova, N. Y. (2022). Explicit IMF B_y-dependence of energetic protons and the ring current. *Geophysical Research Letters*, *49*(8), e2022GL098031. https://doi.org/10.1029/2022GL098031

Holappa, L., & Mursula, K. (2018). Explicit IMF B_y dependence in high-latitude geomagnetic activity. *Journal of Geophysical Research: Space Physics*, *123*(6), 4728–4740. https://doi.org/10.1029/2018ja025517

Holappa, L., Reistad, J. P., & Ohma, A. (2023). Comment on "Unraveling the Role of IMF B_x in Driving Geomagnetic Activity" by Kubyshkina et al. *Journal of Geophysical Research: Space Physics*, *128*(10), e2023JA031701. https://doi.org/10.1029/2023JA031701

Holappa, L., Robinson, R. M., Pulkkinen, A., Asikainen, T., & Mursula, K. (2021). Explicit IMF B_y-dependence in geomagnetic activity: Quantifying ionospheric electrodynamics. *Journal of Geophysical Research: Space Physics*, *126*(4), e2021JA029202. https://doi.org/10.1029/2021JA029202

Hu, Z.-J., Ebihara, Y., Yang, H.-G., Hu, H.-Q., Zhang, B.-C., Ni, B., et al. (2014). Hemispheric asymmetry of the structure of dayside auroral oval. *Geophysical Research Letters*, *41*(24), 8696–8703. https://doi.org/10.1002/2014GL062345

Huang, T., Lühr, H., & Wang, H. (2017). Global characteristics of auroral Hall currents derived from the Swarm constellation: Dependences on season and IMF orientation. In *Annales Geophysicae* (Vol. 35, pp. 1249–1268). Copernicus Publications. https://doi.org/10.5194/angeo-35-1249-2017

Iijima, T., & Potemra, T. A. (1976). Field-aligned currents in the dayside cusp observed by Triad. *Journal of Geophysical Research*, *81*(34), 5971–5979. https://doi.org/10.1029/JA081i034p05971

Iijima, T., & Potemra, T. A. (1982). The relationship between interplanetary quantities and Birkeland current densities. *Geophysical Research Letters*, *9*(4), 442–445. https://doi.org/10.1029/gl009i004p00442

Kervalishvili, G. N., & Lühr, H. (2014). Climatology of zonal wind and large-scale FAC with respect to the density anomaly in the cusp region: Seasonal, solar cycle, and IMF B_y dependence. In *Annales Geophysicae* (Vol. 32, pp. 249–261). Copernicus Publications. https://doi.org/10.5194/angeo-32-249-2014

Knight, S. (1973). Parallel electric fields. *Planetary and Space Science*, *21*(5), 741–750. https://doi.org/10.1016/0032-0633(73)90093-7

Korth, H., Zhang, Y., Anderson, B. J., Sotirelis, T., & Waters, C. L. (2014). Statistical relationship between large-scale upward field-aligned currents and electron precipitation. *Journal of Geophysical Research: Space Physics*, *119*(8), 6715–6731. https://doi.org/10.1002/2014JA019961

Kubyshkina, M. V., Semenov, V. S., Tsyganenko, N. A., Wang, X. G., & Kubyshkin, I. V. (2023). Unraveling the role of IMF B_x in driving geomagnetic activity. *Journal of Geophysical Research: Space Physics*, *128*(4), e2022JA031275. https://doi.org/10.1029/2022JA031275

Laundal, K. M., Finlay, C. C., Olsen, N., & Reistad, J. P. (2018). Solar wind and seasonal influence on ionospheric currents from Swarm and CHAMP measurements. *Journal of Geophysical Research: Space Physics*, *123*(5), 4402–4429. https://doi.org/10.1029/2018JA025387

Laundal, K. M., & Østgaard, N. (2009). Asymmetric auroral intensities in the Earth's Northern and Southern hemispheres. *Nature*, *460*(7254), 491–493. https://doi.org/10.1038/nature08154

Liou, K., & Mitchell, E. J. (2019). Hemispheric asymmetry of the premidnight aurora associated with the dawn-dusk component of the interplanetary magnetic field. *Journal of Geophysical Research: Space Physics*, *124*(3), 1625–1634. https://doi.org/10.1029/2018JA025953

Liou, K., & Mitchell, E. J. (2020). Hemispheric asymmetry of the dayside aurora due to imbalanced solar insolation. *Scientific Reports*, *10*(1), 13451. https://doi.org/10.1038/s41598-020-70018-w

Liu, J., Burns, A. G., Wang, W., & Zhang, Y. (2020). Modeled IMF B_y effects on the polar ionosphere and thermosphere coupling. *Journal of Geophysical Research: Space Physics*, *125*(3), e2019JA026949. https://doi.org/10.1029/2019JA026949

Lühr, H., Ritter, P., Kervalishvili, G., & Rauberg, J. (2020). Applying the dual-spacecraft approach to the swarm constellation for deriving radial current density. In *Ionospheric Multi-spacecraft analysis tools: Approaches for deriving ionospheric parameters* (pp. 117–140).

Lyatskaya, S., Lyatsky, W., & Khazanov, G. V. (2014). Effect of interhemispheric field-aligned currents on region-1 currents. *Geophysical Research Letters*, *41*(11), 3731–3737. https://doi.org/10.1002/2014GL060413

McDiarmid, I. B., Burrows, J. R., & Wilson, M. D. (1979). Large-scale magnetic field perturbations and particle measurements at 1400 km on the dayside. *Journal of Geophysical Research*, *84*(A4), 1431–1441. https://doi.org/10.1029/JA084iA04p01431

Moen, J., & Brekke, A. (1993). The solar flux influence on quiet time conductances in the auroral ionosphere. *Geophysical Research Letters*, *20*(10), 971–974. https://doi.org/10.1029/92GL02109

Newell, P. T., Meng, C. I., & Lyons, K. M. (1996). Suppression of discrete aurorae by sunlight. *Nature*, *381*(6585), 766–767. https://doi.org/10.1038/381766a0

Newell, P. T., Sotirelis, T., Liou, K., Meng, C. I., & Rich, F. J. (2007). A nearly universal solar wind-magnetosphere coupling function inferred from 10 magnetospheric state variables. *Journal of Geophysical Research*, *112*(A1), A01206. https://doi.org/10.1029/2006JA012015

Olsen, N. (1996). A new tool for determining ionospheric currents from magnetic satellite data. *Geophysical Research Letters*, *23*(24), 3635–3638. https://doi.org/10.1029/96GL02896

Østgaard, N., Laundal, K. M., Juusola, L., Åsnes, A., Håland, S. E., & Weygand, J. M. (2011). Interhemispherical asymmetry of substorm onset locations and the interplanetary magnetic field. *Geophysical Research Letters*, *38*(8), L08104. https://doi.org/10.1029/2011GL046767

Pakhotin, I. P., Mann, I. R., Xie, K., Burchill, J. K., & Knudsen, D. J. (2021). Northern preference for terrestrial electromagnetic energy input from space weather. *Nature Communications*, *12*(1), 199. https://doi.org/10.1038/s41467-020-20450-3

Reistad, J. P., Laundal, K. M., Ohma, A., Moretto, T., & Milan, S. E. (2020). An explicit IMF B_y dependence on solar wind-magnetosphere coupling. *Geophysical Research Letters*, *47*(1), e2019GL086062. https://doi.org/10.1029/2019GL086062

Reistad, J. P., Laundal, K. M., Østgaard, N., Ohma, A., Burrell, A. G., Hatch, S. M., et al. (2021). Quantifying the lobe reconnection rate during dominant IMF B_y periods and different dipole tilt orientations. *Journal of Geophysical Research: Space Physics*, *126*(11), e2021JA029742. https://doi.org/10.1029/2021JA029742

Richmond, A. D. (1995). Ionospheric electrodynamics using magnetic apex coordinates. *Journal of Geomagnetism and Geoelectricity*, *47*(2), 191–212. https://doi.org/10.5636/jgg.47.191

Ritter, P., Lühr, H., Maus, S., & Viljanen, A. (2004). High-latitude ionospheric currents during very quiet times: Their characteristics and predictability. In *Annales Geophysicae* (Vol. 22, pp. 2001–2014). https://doi.org/10.5194/angeo-22-2001-2004

Ritter, P., Lühr, H., & Rauberg, J. (2013). Determining field-aligned currents with the Swarm constellation mission. *Earth Planets and Space*, *65*(11), 1285–1294. https://doi.org/10.5047/eps.2013.09.006

Robinson, R. M., Kaeppler, S. R., Zanetti, L., Anderson, B., Vines, S. K., Korth, H., & Fitzmaurice, A. (2020). Statistical relations between auroral electrical conductances and field-aligned currents at high latitudes. *Journal of Geophysical Research: Space Physics*, *125*(7), e2020JA028008. https://doi.org/10.1029/2020ja028008

Russell, C. T., & McPherron, R. (1973). Semiannual variation of geomagnetic activity. *Journal of Geophysical Research*, *78*(1), 92–108. https://doi.org/10.1029/JA078i001p00092

Sato, T., & Iijima, T. (1979). Primary sources of large-scale Birkeland currents. *Space Science Reviews*, *24*(3), 347–366. https://doi.org/10.1007/BF00212423

Smith, A. R. A., Beggan, C. D., Macmillan, S., & Whaler, K. A. (2017). Climatology of the auroral electrojets derived from the along-track gradient of magnetic field intensity measured by POGO, Magsat, CHAMP, and Swarm. *Space Weather*, *15*(10), 1257–1269. https://doi.org/10.1002/2017SW001675

Stenbaek-Nielsen, H. C., & Otto, A. (1997). Conjugate auroras and the interplanetary magnetic field. *Journal of Geophysical Research*, *102*(A2), 2223–2232. https://doi.org/10.1029/96JA03563

Stenbaek-Nielsen, H. C., Wescott, E. M., Davis, T. N., & Peterson, R. W. (1973). Differences in auroral intensity at conjugate points. *Journal of Geophysical Research*, *78*(4), 659–671. https://doi.org/10.1029/JA078i004p00659

Taguchi, S., Sugiura, M., Winningham, J. D., & Slavin, J. A. (1993). Characterization of the IMF B_y-dependent field-aligned currents in the cleft region based on DE 2 observations. *Journal of Geophysical Research*, *98*(A2), 1393–1407. https://doi.org/10.1029/92JA01014

Vennerstrøm, S., Moretto, T., Olsen, N., Friis-Christensen, E., Stampe, A. M., & Watermann, J. F. (2002). Field-aligned currents in the dayside cusp and polar cap region during northward IMF. *Journal of Geophysical Research*, *107*(A8), SMP-18. https://doi.org/10.1029/2001JA009162

Vennerstrom, S., Moretto, T., Rastätter, L., & Raeder, J. (2005). Field-aligned currents during northward interplanetary magnetic field: Morphology and causes. *Journal of Geophysical Research*, *110*(A6), A06205. https://doi.org/10.1029/2004JA010802

Wang, H., & Lühr, H. (2023). Magnetic local time and longitudinal variations of field-aligned currents and polar auroral electrojet. *Journal of Geophysical Research: Space Physics*, *128*(10), e2023JA031874. https://doi.org/10.1029/2023JA03187

Wang, H., & Lühr, H. (2024). IMF B_y effects on the strength and latitude of polar electrojets: CHAMP and swarm joint observations. *Journal of Geophysical Research: Space Physics*, *128*, e2023JA032049. https://doi.org/10.1029/2023JA032049

Wang, H., Lühr, H., & Ma, S. Y. (2005). Solar zenith angle and merging electric field control of field-aligned currents: A statistical study of the Southern Hemisphere. *Journal of Geophysical Research*, *110*(A3), A03306. https://doi.org/10.1029/2004JA010530

Wang, H., Lühr, H., Shue, J.-H., Frey, H. U., Kervalishvili, G., Huang, T., et al. (2014). Strong ionospheric field-aligned currents for radial interplanetary magnetic fields. *Journal of Geophysical Research*, *119*(5), 3979–3995. https://doi.org/10.1002/2014JA019951

Wang, H., Ridley, A. J., & Lühr, H. (2008). SWMF simulation of field-aligned currents for a varying northward and duskward IMF with nonzero dipole tilt. *Annales Geophysicae*, *26*(6), 1461–1477. https://doi.org/10.5194/angeo-26-1461-2008

Wang, Z., & Zou, S. (2022). COMPASS: A new COnductance Model based on PFISR And SWARM Satellite observations. *Space Weather*, *20*(2), e2021SW002958. https://doi.org/10.1029/2021SW002958

Workayehu, A. B., Vanhamäki, H., Aikio, A. T., & Shepherd, S. G. (2021). Effect of interplanetary magnetic field on hemispheric asymmetry in ionospheric horizontal and field-aligned currents during different seasons. *Journal of Geophysical Research: Space Physics*, *126*(10), e2021JA029475. https://doi.org/10.1029/2021JA029475

Yamauchi, M., Lundin, R., & Woch, J. (1993). The interplanetary magnetic field B_y effects on large-scale field-aligned currents near local noon: Contributions from cusp part and noncusp part. *Journal of Geophysical Research*, *98*(A4), 5761–5767. https://doi.org/10.1029/92ja02934

Zhao, H., & Zong, Q. G. (2012). Seasonal and diurnal variation of geomagnetic activity: Russell-McPherron effect during different IMF polarity and/or extreme solar wind conditions. *Journal of Geophysical Research*, *117*(A11), A11222. https://doi.org/10.1029/2012ja017845

Zhou, Y. L., & Lühr, H. (2017). Net ionospheric currents closing field-aligned currents in the auroral region: CHAMP results. *Journal of Geophysical Research: Space Physics*, *122*(4), 4436–4449. https://doi.org/10.1002/2016JA023090